
A Load Balance Strategy for Hybrid Particle-Mesh Methods

P. Ortwein¹, T. Binder², S. Copplestone¹, A. Mirza², P. Nizenkov²,
M. Pfeiffer², C.-D. Munz¹, and S. Fasoulas²

¹ Institute of Aerodynamics and Gas Dynamics (IAG), University of Stuttgart,
70569 Stuttgart, Germany munz@iag.uni-stuttgart.de

² Institute of Space Systems (IRS), University of Stuttgart, 70569 Stuttgart,
Germany fasoulas@irs.uni-stuttgart.de

Summary. We present a load balancing strategy for hybrid particle-mesh methods that is based on domain decomposition and element-local time measurement. This new strategy is compared to our previous approach, which assumes a constant weighting factor for each particle to determine the computational load. The timer-based load balancing is applied to a plasma expansion simulation. The performance of the new algorithm is compared to results presented in the past and a significant improvement in terms of computational efficiency is shown.

1 Introduction

In highly parallelized simulation methods that are based on both particle and spatial discretization techniques, such as Particle-in-Cell (PIC) and Direct Simulation Monte Carlo (DSMC), load imbalance is inevitable. As soon as the particle distribution is inhomogeneous or certain types of boundary conditions are encountered, the load increases for certain regions within the computational domain. To avoid inefficient resource utilization, this problem has to be addressed, for example by using a flexible domain decomposition approach. In the following, the newest development of the PICLas code [7] concerning load balance concepts is presented. The approach is similar to the one presented in [2], where timers are used for determining a global ratio

by calculating a particle-element weighting factor. A fixed value concept has therefore been implemented in previous versions of PICLas [9]. However, a restriction of the redistribution scheme to a global particle-weighting factor is not suitable for all simulation scenarios. Therefore, individual weights on an element level, which are determined dynamically during the simulation, are used in the present work. Other known load balance concepts for PIC migrate particles between MPI processes [10] or utilize a general particle-field decomposition approach [11]. Most recently, a load-management strategy was proposed in [1], including an improved data structure [4] that enables an efficient distribution of the load, which is broken into individual segments. This approach is well suited for an efficient dynamic load distribution, similar to the element sorting along a space filling curve (SFC) in PICLas.

After a brief review of the underlying PIC theory in Sec. 2, the load computation and distribution concept is discussed in Sec. 3. The results are presented in Sec. 4 and the paper is concluded by a summary and outlook on future code developments in Sec. 5.

2 Particle-in-Cell Theory

The well-known PIC method is typically used to find an approximate solution of the collision-free Boltzmann equation, which is also called the Vlasov equation:

$$\frac{\partial f_\alpha}{\partial t} + \mathbf{v}_\alpha \frac{\partial f_\alpha}{\partial \mathbf{x}_\alpha} + \frac{\mathbf{F}}{m_\alpha} \frac{\partial f_\alpha}{\partial \mathbf{v}_\alpha} = 0 . \quad (1)$$

Here, $f_\alpha = f_\alpha(\mathbf{x}, \mathbf{v}, t)$ is the particle distribution function of species α at the position \mathbf{x} and time t with velocity \mathbf{v} . Additionally, m is the particle mass, and \mathbf{F} is the Lorentz force, given by

$$\mathbf{F} = q_\alpha (\mathbf{E} + \mathbf{v}_\alpha \times \mathbf{B}) , \quad (2)$$

with the particle charge q , the electric field \mathbf{E} and the magnetic field \mathbf{B} . The electromagnetic fields \mathbf{E} and \mathbf{B} are solutions of the Maxwell's equations

$$\frac{\partial \mathbf{E}}{\partial t} - c^2 \nabla \times \mathbf{B} = -\frac{\mathbf{j}}{\epsilon_0} , \quad (3)$$

$$\frac{\partial \mathbf{B}}{\partial t} + \nabla \times \mathbf{E} = 0 , \quad (4)$$

$$\nabla \cdot \mathbf{E} = \frac{\rho}{\epsilon_0} , \quad (5)$$

$$\nabla \cdot \mathbf{B} = 0 . \quad (6)$$

The corresponding source terms are the charge density ρ and the current density \mathbf{j} , defined as moments of the distribution function by

$$\begin{aligned} \rho(\mathbf{x}, t) &= q \int_{\mathbb{R}^3} f(\mathbf{x}, \mathbf{v}, t) d^3v , \\ \mathbf{j}(\mathbf{x}, t) &= q \int_{\mathbb{R}^3} \mathbf{v} f(\mathbf{x}, \mathbf{v}, t) d^3v . \end{aligned} \quad (7)$$

The main idea of PIC methods is to approximate the distribution function by a discrete number of particles, which are mathematically described by the linear combination of N δ -functions with a super-particle weighting factor w_k

$$f(\mathbf{x}, \mathbf{v}, t) \approx \sum_{k=1}^N w_k \delta(\mathbf{x} - \mathbf{x}_k(t)) \delta(\mathbf{v} - \mathbf{v}_k(t)) . \quad (8)$$

Due to this approximation and the corresponding numerical errors, it is not sufficient to solely solve equations (3) and (4), although they are mathematically well-defined for appropriate boundary and initial conditions. Owing to numerical errors, an additional unphysical divergence term appears. Consequently, equations (5) and (6) are no longer fulfilled. To overcome this problem, a purely hyperbolic formulation of Maxwell's equations (PHM) is solved as described in [8]. The system of equations is given by

$$\frac{\partial \mathbf{E}}{\partial t} = c^2 \nabla \times \mathbf{B} - \frac{\mathbf{j}}{\epsilon_0} - \chi c^2 \nabla \Psi , \quad (9)$$

$$\frac{\partial \mathbf{B}}{\partial t} = -\nabla \times \mathbf{E} - \chi \nabla \Theta , \quad (10)$$

$$\frac{\partial \Psi}{\partial t} = \chi \left(-\nabla \cdot \mathbf{E} + \frac{\rho}{\epsilon_0} \right) , \quad (11)$$

$$\frac{\partial \Theta}{\partial t} = -\chi c^2 \nabla \cdot \mathbf{B} , \quad (12)$$

with the dimensionless positive parameter χ and the generalized Lagrange multipliers $\Psi(\mathbf{x}, t)$ and $\Theta(\mathbf{x}, t)$, where the latter two properties are scalar potential fields. These additional variables couple the divergence conditions (5)

and (6) to the evolution equations (3) and (4). The PHM system is solved using a Discontinuous Galerkin Spectral Element Method (DGSEM) as described in [7]. In the following, a short introduction to this method is given. For the DG method, the simulation region Ω is split into non-overlapping grid cells Ω_i in which the approximation of the solution is a continuous function, usually a piecewise polynomial function. To solve equations (9)-(12), they are re-written in conservation form

$$\frac{\partial \mathbf{U}}{\partial t} + \nabla \cdot \mathbf{F}(\mathbf{U}) = \mathbf{S} , \quad (13)$$

where \mathbf{F} represents the physical flux vector, \mathbf{U} the solution and \mathbf{S} the source terms, which are given by

$$\mathbf{U} = (\mathbf{E}, \mathbf{B}, \psi, \Theta)^T , \quad (14)$$

and

$$\mathbf{S} = \frac{1}{\varepsilon_0} (\mathbf{j}, \mathbf{0}, \chi\rho, 0)^T , \quad (15)$$

respectively. In the DGSEM context, equation (13) is transformed from the physical space Ω to the reference space $\mathcal{E} \in [-1, 1]^3$ giving

$$\frac{\partial \mathbf{U}}{\partial t} + \frac{1}{J} \nabla_{\xi} \cdot \tilde{\mathbf{F}} = \mathbf{S} , \quad (16)$$

where J is the Jacobian determinant of the transformation, ∇_{ξ} the divergence operator with respect to the reference space and $\tilde{\mathbf{F}}$ the transformed flux vector. This equation is multiplied by a test function ϕ and integrated over \mathcal{E} leading to

$$\int_{\mathcal{E}} J \frac{\partial \mathbf{U}}{\partial t} \phi \, d\xi + \underbrace{\int_{\partial \mathcal{E}} \tilde{\mathbf{F}} \cdot \mathbf{N} \phi \, ds}_{\text{Surface Integral}} - \underbrace{\int_{\mathcal{E}} \tilde{\mathbf{F}} \cdot \nabla_{\xi} \phi \, d\xi}_{\text{Volume Integral}} = \int_{\mathcal{E}} J \mathbf{S} \phi \, d\xi , \quad (17)$$

where integration by parts has been used to split the divergence integral into a surface and a volume integral. The advantage of this method in the context of parallelization is that only the surface integral is responsible for the inter-cell coupling between DGSEM cells. Using MPI parallelization, the only messages that have to be communicated arise from this surface integral. This leads to a highly efficient scheme with remarkable scaling properties in high performance computing (HPC) contexts [5].

3 Load Balance Strategy

The present load measurement strategy is applicable for two reasons: Firstly, the high-order DG method as used and, secondly, an explicit time-stepping. As the use of high-order discretization tends to enlarge elements, a particle remains in a certain element for a longer period of time. This justifies the utilization of a previously determined distribution over a certain simulation period. In the following, the load computation and distribution scheme is presented in detail.

3.1 Load Computation

In order to distribute the load between different processes, the total load L_{tot} has to be determined. It is computed by adding up the load L_i that is ascertained for each individual element

$$L_{\text{tot}} = \sum_{i=1}^{n_{\text{Elements}}} L_i . \quad (18)$$

In a perfectly balanced simulation, each MPI process receives the average load

$$L_{\text{average}} = \frac{L_{\text{tot}}}{n_{\text{Process}}} , \quad (19)$$

with n_{Process} being the number of MPI processes. The load per element L_i can be determined by different methods: particle weighting or runtime measurements. The first idea uses a fixed weight ν for each particle. Hence, the load of each cell is calculated by

$$L_i = 1 + \nu n_{\text{Part}} , \quad (20)$$

where the assumed constant load of the DG operator is increased by νn_{Part} , which is the particle-element weight multiplied by the number of particles that reside in each cell. The latter is run-time dependent and represents merely a rule of thumb. Fixed particle weights are simple to implement. However, they have to be determined for each simulation scenario. Amongst others, they depend on the number of simulated particles and boundary interactions. Runtime measurements, on the other hand, are more flexible, allowing to compute the particle-element weight during the simulation, which inherently

considers inhomogeneous particle distributions and varying computational effort within the domain. The measurement utilized here exclusively contains computational time; hence, MPI communication is not considered. MPI communication and process-idle time depend on the current load distribution and are neglected, since an ideal non-blocking communication should introduce no overheads. To account for region-dependent loads, runtime measurement is not performed at process level, but rather the computational time for each element t_e is measured. In this work, the total computation time for each element consists of different components for each module and is defined as

$$t_e = t_{m,\text{Field}} + t_{m,\text{Particle}} , \quad (21)$$

with $t_{m,\text{Field}}$ being the time for the field solver and $t_{m,\text{Particle}}$ the time for the particle treatment. For $t_{m,\text{Field}}$, the time is measured in total for each process and the process average time is assigned to each element, assuming the required computational effort is similar for each cell. In contrast, $t_{m,\text{Particle}}$ depends on the considered element. The time measurement directly provides the load distribution throughout the computational domain. In a next step, the load of each element is set equal to the measured time

$$L_i = t_e , \quad (22)$$

and the load is distributed as described in the following section. After a specific time interval or number of iterations, the current load is compared with the last measured load and if the deviation

$$\Delta L = \frac{L_{tot,old} - L_{tot,new}}{L_{tot,old}} > \alpha , \quad (23)$$

is above a threshold α , a load distribution step is performed.

3.2 Load Distribution

The load distribution between the MPI processes is a crucial step. If the load is not distributed homogeneously, the load balancing effect is limited. In a preprocessing step, all elements within the computational domain are sorted along a Hilbert curve due to its clustering property [6]. Then, each MPI process receives a certain segment of the SFC. To illustrate an optimal load balance

scenario, a simplified grid is considered that consists of $8 \times 8 = 64$ elements, which are ordered along a SFC. Fig. 1a depicts the decomposition of the grid into four regions, each corresponding to an individual MPI process. Without particles, no load imbalance is observed. Next, in the lower left and upper right corner, four particles are inserted thus increasing the total computational weight from 64 to 72 (arbitrary units) using a particle-element weight of 2. A domain decomposition algorithm is then applied and the elements and its particles are assigned to a certain process. To maintain load balance, the size of two empty regions has to increase, whereas the other two have to decrease, which is achieved by moving the element assignment along the SFC to the next MPI process. The results of this balancing step are shown in Fig. 1b, and the total domain still remains balanced. However, the introduction of the load imbalance at the element level yields additional difficulties. The first case can be distributed among $\{2, 4, 8, 16, 32, 64\}$ MPI processes, whereas the latter, imbalanced case can only be distributed on $\{2, 4, 8\}$ processes in order to be fully balanced. This example demonstrates different aspects. The load has to be assigned carefully, possible load imbalances reduce the total number of applicable MPI processes and therefore the load balance may not be guaranteed for all cases. From these considerations, specifications for the load

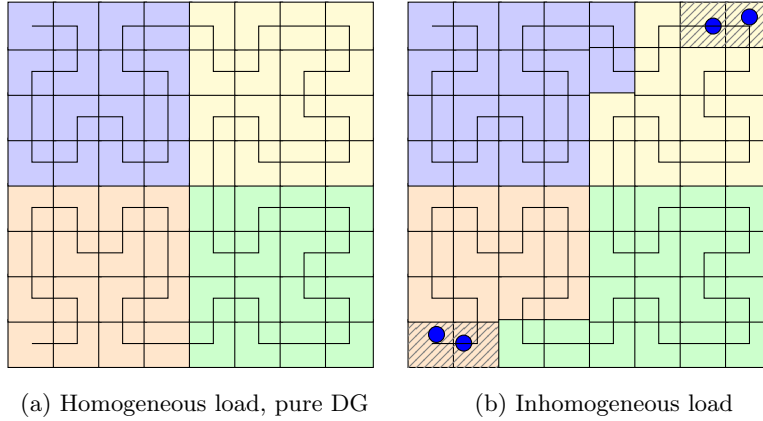


Fig. 1: Domain decomposition via SFC ordering.

distribution algorithm can be defined, e.g., it has to satisfy the following two conditions

1. Minimize the load deviation,
2. Prevent the last process from receiving too much load (above average).

By applying the first condition, each process p receives a load

$$L_p = \left| L_{\text{target}} - \sum_{i_{\text{low}}}^{i_{\text{up}}} L_i \right| \stackrel{!}{=} \min, \quad (24)$$

where i_{low} is the lower element index that is not assigned previously to a certain MPI process. Here, i_{up} is the upper element index assigned to process p that is chosen to minimize the deviation from the average load for this process. Next, it is examined if the last MPI process receives a load larger than the average value. If this condition is satisfied, then the mean deviation is increased by the load difference

$$L_{\text{target}}^0 = L_{\text{mean}}, \quad L_{\text{target}}^{i+1} = L_{\text{target}}^i + \frac{L_{\text{last}} - L_{\text{target}}^i}{n_{\text{Process}}}, \quad (25)$$

and the load distribution step is repeated. The second condition guarantees that the last process receives a smaller value than the average load. Thus, not acquiring too much load prevents the introduction of a load imbalance by the distribution algorithm. In an optimally balanced case, each process receives approximately the average load. Due to the sequential load distribution, it cannot be guaranteed that the last process receives the average load. Hence, it must be prevented that the last process receives a load larger than the average in order to circumvent idle time.

4 Results

A plasma plume setup from [3] is revised to investigate the improvements of the new load balancing concept. The setup consists of a cylindrical plasma (radius $r = 20\mu\text{m}$, height $h_z = 70\mu\text{m}$ in z -direction) that is placed inside a cuboid domain of $\Delta x \times \Delta y \times \Delta z = 120\mu\text{m} \times 120\mu\text{m} \times 210\mu\text{m}$. This results in a heterogeneous particle distribution and consequently in a heterogeneously distributed load. The presented results consider a small simulation time t_{sim}

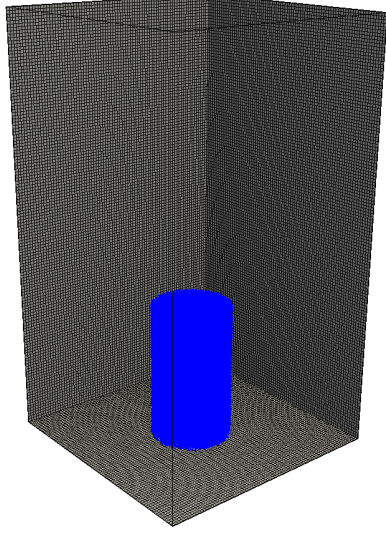


Fig. 2. Initial particle distribution and cuboid grid utilizing $80 \times 80 \times 140$ cells.

within which the particles movement does not lead to a significant change in spatial load distribution, thus, the static load balance limit is investigated. Additionally, the cases are pure PIC simulations without DSMC routines. It is examined whether the load can be distributed for a given number of cells and particles among the chosen number of MPI processes, where each process is always assigned to a single core. The initial conditions of both setups are given in Table 1. The algorithms parallel performance is measured by

Table 1: Initial Conditions

Property	Case A	Case B
Particle number	$N_{e-} = N_{Al+} = 1 \cdot 10^5$	$N_{e-} = N_{Al+} = 1 \cdot 10^6$
Electron density	$n_{e-} = 5 \cdot 10^{24} \text{ m}^{-3}$	$n_{e-} = 3.41 \cdot 10^{23} \text{ m}^{-3}$
Simulation particle weight	$w_k \approx 4.4 \cdot 10^6$	$w_k \approx 3.0 \cdot 10^4$
Electron temperature	$T_{e-} = 2 \cdot 10^4 \text{ K}$	$T_{e-} = 1.16 \cdot 10^7 \text{ K}$
Ion temperature	$T_{Al+} = 1 \cdot 10^4 \text{ K}$	$T_{Al+} = 1.16 \cdot 10^5 \text{ K}$
Debye length	$\lambda_D = 2.52 \cdot 10^{-9} \text{ m}$	$\lambda_D = 4.0 \cdot 10^{-7} \text{ m}$
Polynomial degree	6	3

$$\tau = \frac{t_{\text{sim}}}{N_{\text{proc}} t_{\text{wall}}} , \quad (26)$$

where t_{sim} is the simulated time difference, t_{wall} the wall clock time (without I/O and initialization) and N_{proc} the number of processes utilized within the simulation. It relates the simulation time to the employed resources, which are the total number of CPU hours used for a simulation. Fig. 3 illustrates the results obtained for two different deposition methods, a delta distribution and a shape function and compares them to the previous code version [3]. For the δ -function deposition, the new code performs similarly to the old version. However, when a shape-function is utilized the performance increases. In this example, the new code outperforms the previous version by a factor of three, presumably, due to latency hiding. For $N_{\text{proc}} \leq 4800$, the performance is kept at a constant level and when $N_{\text{proc}} > 4800$, the problem size (memory requirement) for each MPI domain is decreased for which caching effects lead to an even better performance. As soon as the one cell per MPI domain limit is reached, the work within this cell cannot be parallelized in the current framework and currently represents the algorithm's barrier. Fig. 4 depicts

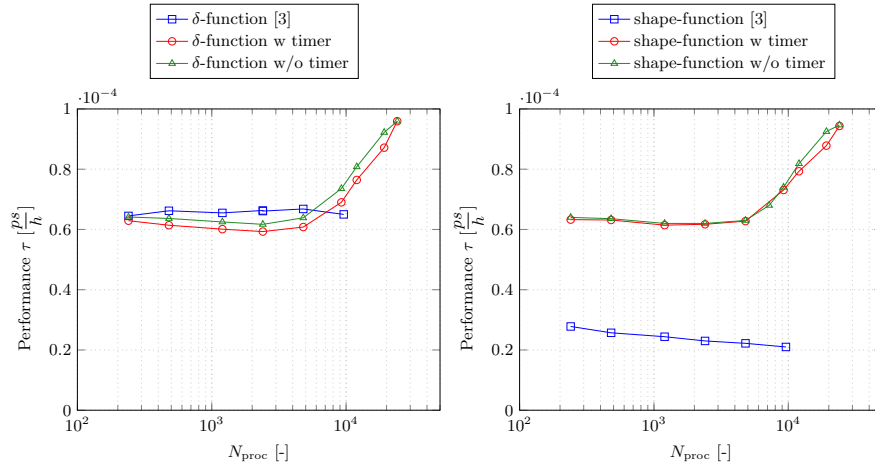


Fig. 3: Code peak performance for two deposition techniques as compared with [3], where the number of processes chosen were between 240 and 24000 (Case A).

the parallel strong scaling of the code up to 24,000 cores for the new and old

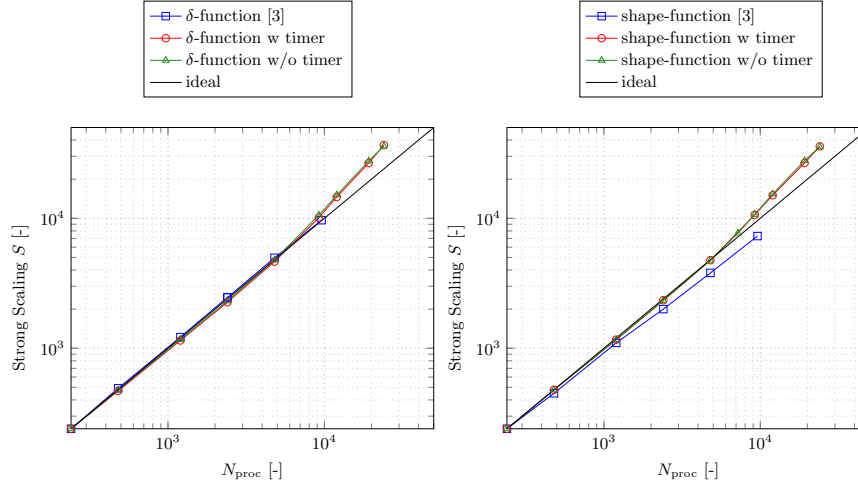


Fig. 4: Optimum strong scaling for two deposition techniques as compared with [3], where the number of processes chosen were between 240 and 24000 (Case A).

version of the code, which relates the speed-up due to parallelization

$$S = \frac{240 \cdot t_{240}}{t_{N_{\text{proc}}}} , \quad (27)$$

where t_{240} is the wall time for a simulation with a minimum number of 10 compute nodes, each yielding 24 physical cores, as they offer the minimum amount of memory required for the test case and $t_{N_{\text{proc}}}$ is the simulation time for a setup with N_{proc} processes. For the next setup, the polynomial degree is reduced to $N = 3$ and the number of particles per species is increased by a factor of ten to increase the computational load of the particles. The left-hand diagram of Fig. 5 depicts a slice in the $x - z$ -plane and shows the computational time per DG element. The inner region is particle-laden, and each element is roughly one hundred times more expensive than a pure DG element. Additionally, the computational time shows variation for pure DG elements. The right-hand graph in Fig. 5 illustrates the performance with and without the element time measurement. A fixed particle-element weight ($\nu = 0.02$) results in a constant performance distribution over the investigated range of MPI processes (240 to 9216). In contrast, the performance decreases with higher number of MPI processes when a timer is utilized. Nevertheless,

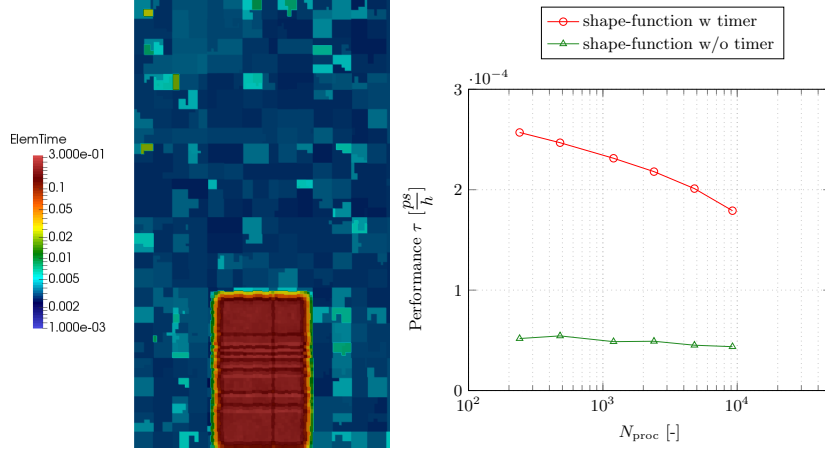


Fig. 5: Initially measured load distribution in the x - z -plane (left) and code peak performance with and without load measurement, where the number of processes chosen were between 240 and 9216 (Case B).

the performance is more than three to five times higher than without time measurement. For illustrating the scaling characteristics in more detail, Fig. 6

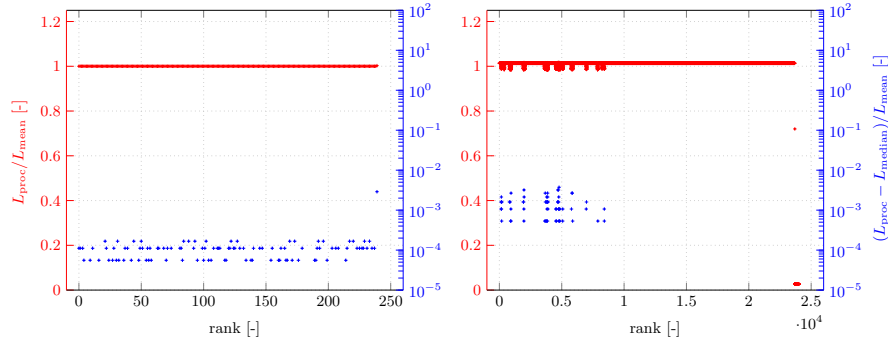


Fig. 6: Relative measured load (Case A) over MPI ranks (red) and positive deviation from median in logarithmic scale (blue), and the number of processes are 240 (left) and 24000 (right).

and Fig. 7 depict partition information regarding measured loads of assigned elements for the smallest and largest number of MPI ranks chosen for Case A and B respectively. It has to be mentioned that the loads are those utilized

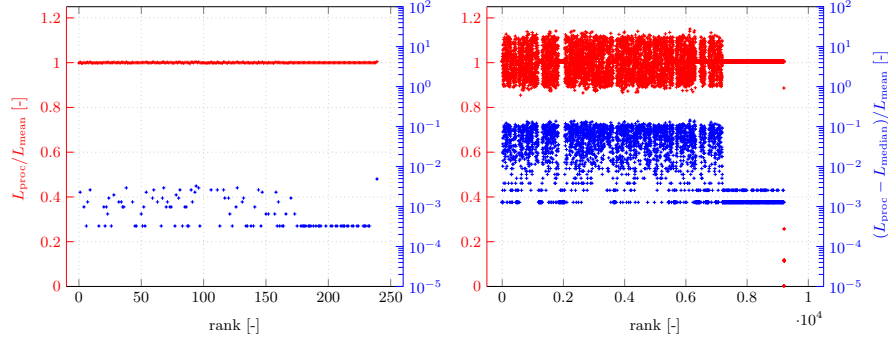


Fig. 7: Relative measured load (Case B) over MPI ranks (red) and positive deviation from median in logarithmic scale (blue), and the number of processes are 240 (left) and 9216 (right).

for the distribution, however they may differ from the actual loads of the subsequent calculations. Fig. 6 shows that for Case A, the assigned loads of all processes scaled by the mean value (red dots) are within a narrow band around unity. The relative deviations in logarithmic scale show that for the processes with a load greater than the median (blue dots) the deviations are below one percent. When neglecting the single anomalous point for the last MPI ranks, the deviation is on the order of $1 \cdot 10^{-4}$ for the case with 240 processes. The reason and impact of the increased load of the last process is subject to ongoing investigations. All in all, the small deviations of the processes with a larger load than the median, results in an even load distribution and small idling times of processes. In contrast, Fig. 7 illustrates that for Case B the load is distributed less homogeneously. For 240 processes, the relative positive deviation increases to an order of $1 \cdot 10^{-3}$ and for 9216 processes to $1 \cdot 10^{-1}$. This significant deviation for a large number of processes leads to an idling of the remaining system and, thus, a decreased performance. As exactly those processes deviating from the average load band are containing the particles, it is evident that the increased load inhomogeneity is due to the accumulated particle time, which is now, at least, in the order of the more homogeneous DG time. The band-width of the load deviation could be reduced by shifting elements to larger ranks, where no particles are included. However, this would only have a limited impact as those processes constitute only one forth, while

the even smaller ratio of particle-laden elements are only clustered in isolated sections of the space filling curve.

5 Summary and Conclusions

In this paper, we have presented a load balancing strategy based on time measurement, where the pure computational time per element was determined. The computational effort consists of an approximately constant part for the field solver and a dynamic part for the particle treatment. To cope with the dynamically changing load, which cannot be determined a priori, the computational time was measured in each cell of the domain. This enables an improved load balance over a wide range of applications. The new load balance strategy is applied to a plasma expansion scenario [3]. The case demonstrates the load imbalance problem with a constant particle-element weight and an increasing particle-element ratio. A significant improvement of the performance can be achieved by pursuing the time measurement strategy. Nonetheless, single elements assigned to single MPI processes can make a homogeneous load distribution impossible. This is especially encountered for a large number of MPI processes, where a large number of particles accumulate in individual elements. A possible solution is a hybrid parallelization approach utilizing OpenMP, allowing for larger MPI domains and thus efficiently moving the scaling limit to a higher number of CPUs. In the future, the presented load balance strategy will be applied to coupled PIC-DSMC simulations, which typically exhibit a strong load imbalance.

6 Acknowledgements

We gratefully acknowledge the Deutsche Forschungsgemeinschaft (DFG) for funding within the projects "Kinetic Algorithms for the Maxwell-Boltzmann System and the Simulation of Magnetospheric Propulsion Systems" and "Coupled PIC-DSMC-Simulation of Laser Driven Ablative Gas Expansions". The latter being a sub project of the Collaborative Research Center (SFB) 716 at the University of Stuttgart. Computational resources have been provided by the Bundes-Höchstleistungsrechenzentrum Stuttgart (HLRS).

References

1. Arnaud Beck, J.T. Frederiksen, and J. Dérouillat. Load management strategy for Particle-In-Cell simulations in high energy particle acceleration. Nuclear Instruments and Methods in Physics Research Section A: Accelerators, Spectrometers, Detectors and Associated Equipment, 2016.
2. Matthew T. Bettencourt and Andrew D. Greenwood. Performance improvements for efficient electromagnetic particle-in-cell computation on 1000s of CPUs. IEEE Transactions on Antennas and Propagation, 56(8):2178–2186, 2008.
3. S. Copplestone, T. Binder, A. Mirza, P. Nizenkov, P. Ortwein, M. Pfeiffer, S. Fasoulas, and C.-D. Munz. Coupled PIC-DSMC Simulations of a Laser-driven Plasma Expansion. In Wolfgang E. Nagel, Dietmar H. Kröner, and Michael M. Resch, editors, High Performance Computing in Science and Engineering ‘15. Springer International Publishing, 2016.
4. Kai Germaschewski, William Fox, Narges Ahmadi, Liang Wang, Stephen Abbott, Hartmut Ruhl, and Amitava Bhattacharjee. The Plasma Simulation Code: A modern particle-in-cell code with load-balancing and GPU support. arXiv, pages 1–34, 2013.
5. F. Hindenlang, G. J. Gassner, C. Altmann, A. Beck, M. Staudenmaier, and C.-D. Munz. Explicit discontinuous Galerkin methods for unsteady problems. Comput. Fluids, 61:69–93, may 2012.
6. B. Moon, H.V. Jagadish, C. Faloutsos, and J.H. Saltz. Analysis of the clustering properties of the Hilbert space-filling curve. Knowledge and Data Engineering, IEEE Transactions on, 13(1):124–141, Jan 2001.
7. C.-D. Munz, M. Auweter-Kurtz, S. Fasoulas, A. Mirza, P. Ortwein, M. Pfeiffer, and T. Stindl. Coupled Particle-In-Cell and Direct Simulation Monte Carlo method for simulating reactive plasma flows. Comptes Rendus Mécanique, 342(10-11):662–670, October 2014.
8. C.-D. Munz, P. Omnes, and R. Schneider. A three-dimensional finite-volume solver for the Maxwell equations with divergence cleaning on unstructured meshes. Computer Physics Communications, 130:83 – 117, 2000.
9. P. Ortwein, T. Binder, S. Copplestone, A. Mirza, P. Nizenkov, M. Pfeiffer, T. Stindl, S. Fasoulas, and C.-D. Munz. Parallel Performance of a Discontinuous Galerkin Spectral Element Method Based PIC-DSMC Solver. In Wolfgang E. Nagel, Dietmar H. Kröner, and Michael M. Resch, editors, High Performance Computing in Science and Engineering ‘14, pages 671–681. Springer International Publishing, 2015.

10. Steven J. Plimpton, David B. Seidel, Michael F. Pasik, Rebecca S. Coats, and Gary R. Montry. A load-balancing algorithm for a parallel electromagnetic particle-in-cell code. Computer Physics Communications, 152(3):227–241, may 2003.
11. Ji Qiang and Xiaoye Li. Particle-field decomposition and domain decomposition in parallel particle-in-cell beam dynamics simulation. Computer Physics Communications, 181(12):2024–2034, dec 2010.